

Atomistic calculation of the thermal conductance of large scale bulk-nanowire junctionsIvan Duchemin^{*} and Davide Donadio[†]*Max Planck Institute for Polymer Research, Ackermannweg 10, D-55128 Mainz, Germany*

(Received 18 March 2011; revised manuscript received 21 July 2011; published 16 September 2011)

We have developed a stable and efficient kernel method to compute thermal transport in open systems, based on the scattering-matrix approach. This method is applied to compute the thermal conductance of a junction between bulk silicon and silicon nanowires with diameter up to 10 nm. We have found that beyond a threshold diameter of 7 nm, transmission spectra and contact conductances scale with the cross section of the contact surface, whereas deviations from this general trend are observed in thinner wires. This result allows us to predict the thermal resistance of bulk-nanowire interfaces with larger cross sections than those tractable with atomistic simulations, and indicate the characteristic size beyond which atomistic systems can in principle be treated accurately by mean-field theories. Our calculations also elucidate how dimensionality reduction and shape affect interfacial heat transport.

DOI: [10.1103/PhysRevB.84.115423](https://doi.org/10.1103/PhysRevB.84.115423)

PACS number(s): 63.22.-m, 66.70.Df, 81.07.Gf, 11.55.-m

I. INTRODUCTION

Nanostructures and nanostructured materials offer the possibility to tune heat transport properties over an exceptionally wide range. For example, in carbon-based materials it is possible to obtain variations of the thermal transport coefficients over three orders of magnitude: Graphene and suspended carbon nanotubes are possibly the most efficient heat conductors,^{1,2} whereas interacting nanotubes, in networks or bundles,^{3,4} and graphene nanoribbons with disordered edges are predicted to have thermal insulating properties.⁵ Similarly, nanostructuring may turn silicon and SiGe alloys into efficient thermoelectric materials by significantly reducing the thermal conductivity (κ) as in the case of nanowires⁶⁻⁸ (SiNW), SiGe nanocomposites,⁹ superlattices,¹⁰ and nanoporous silicon.^{11,12}

Further improvement in designing materials and nanodevices with controlled thermal transport properties stems from a deeper theoretical understanding of phonon transport. Following Landauer and Büttiker's works,^{13,14} atomistic Green's function (GF) formalism has become the reference method to study coherent electronic transport.¹⁵⁻¹⁷ The GF approach has been transferred successfully to compute thermal transport in nanostructures,¹⁸⁻²¹ and it is the optimal framework to investigate elastic phonon scattering from impurities, defects, disorder or interfaces (i.e., in all those cases where anharmonic phonon-phonon scattering can be deemed of secondary importance^{22,23}). An atomistic GF method including phonon-phonon scattering has also been developed and applied to small model systems,²⁴ however, one can in general safely assume elastic scattering when a finite nanoscale system between two reservoirs, connected with coherent junctions, is considered. This is often the case for solid state junctions between materials with similar vibrational spectra. Anharmonic effects may also be neglected in several other cases, such as molecular junctions, grain boundaries, and superlattices, but special care must be taken in testing this assumption. Similarly, one has to use coherent scattering methods in a very critical way when he wants to extrapolate finite size calculations to extended materials, where long wavelength phonons do not get scattered by nanoscale impurities and contribute a significant amount to the total thermal conductivity.

In spite of significant insight achieved in these former studies, it remains a formidable task to perform atomistic simulations of nanostructures with characteristic sizes of several tens of nanometers, as it would be needed to bridge the gap between theory and experiment. Because of matrix inversion operations, even the recursive implementation of the GF method, which permits us to deal with systems extending for several micrometers in the direction of heat propagation, imposes severe size limitations in the orthogonal plane. Even though partitioning and "knitting" algorithms to circumvent this problem have so far been proposed for GF calculations of electronic transport,^{25,26} such schemes have not yet been applied to heat transport. In terms of SiNW, this means that one is limited to diameters that do not exceed a few nanometers.²¹ Similar limitations hamper the predictive power of approaches based on molecular dynamics, so far restrained to the study of thin wires.^{27,28}

Lattice dynamics methods that do not utilize GF for the solution of the phonon transport problem were proposed in the past.²⁹⁻³¹ These methods, compared to those based on GF, replace the calculation of the self-energy with an eigenvalue equation. Here we outline a formalism for phonon transport based on lattice dynamics and the scattering-matrix approach,³² in the same spirit as the scattering boundary equation method proposed in Ref. 31. Our approach circumvents the matrix inversion problem by substituting eigenvalue equations with local kernel search and intersections.

After deriving a generalized scattering-matrix approach for phonon propagation in Sec. II, in Sec. III we will illustrate a numerically stable and efficiently parallelizable kernel method to solve the scattering problem. In Sec. IV we will discuss the application of the scattering formalism to compute the contact thermal resistance between bulk silicon and SiNWs with diameters up to 14 nm.

II. SCATTERING-MATRIX APPROACH

The scattering-matrix approach was formulated to solve quantum electronic transmission problems,^{32,33} and found its natural application for the simulation of scanning tunneling microscopy images³⁴ and of molecular electronic devices via

the so-called *elastic scattering quantum chemistry* (ESQC) method.³³ Here we reformulate the theory in terms of phonon transport, making use of lattice dynamics concepts,^{29,30} extending the one proposed by Wang and Wang³¹ to two parts of a general open system.

We consider a phonon wave packet, represented by a weight-normalized displacement field u , traveling through an open system made of semi-infinite reservoirs connected by an arbitrary structure (defect). Our goal is to determine the thermal energy exchanged between the reservoirs through the defect in stationary nonequilibrium conditions (i.e., when the reservoirs are kept at different temperatures). In the harmonic approximation, the equation of motion for the displacement field $u(t)$ is $\ddot{u}(t) = \mathbf{D}u(t)$, where \mathbf{D} is the force constant matrix. The real-valued state u can be decomposed in terms of the complex valued eigenstates $v(\omega)$ of \mathbf{D} . Given the state $u(t_0)$ and its eigen-decomposition coefficients $g_{\tau_0}(\omega)$, the time propagation of u is

$$u(t) = \int [g_{\tau_0}(\omega)v(\omega)e^{-i\omega(t-\tau_0)} + \text{cc.}]d\omega. \quad (1)$$

Let \mathbf{P} be the projector associated with the degrees of freedom of an arbitrary part P of the system. To get the energy exchanged between P and the rest of the system, one can balance the time derivatives of the work from P to the whole system and vice versa, thus obtaining

$$\dot{E}_P(t) = \langle \dot{u}(t) | [\mathbf{P}, \mathbf{D}] | u(t) \rangle. \quad (2)$$

The energy of P in stationary conditions ($E_P(\infty)$) is found by integrating (2) to the infinite time limit. Substituting u with its eigen decomposition in (1) in the integral leads to

$$E_P(\infty) = -2\pi i \int \hbar\omega |g_{\tau_0}(\omega)|^2 \langle v(\omega) | [\mathbf{P}, \mathbf{D}] | v(\omega) \rangle d\omega. \quad (3)$$

All information concerning the initial state lies in the weights $g_{\tau_0}(\omega)$, which can be taken as the statistical distribution of the states $|v\rangle$ when simulating a system at finite temperature. In the stationary nonequilibrium case, those weights refer to the rate of phonons emitted from the reservoirs [i.e., one-dimensional (1D) phonon gas obeying Bose-Einstein statistics]:

$$|g_0(\omega)|^2 = \frac{1}{2\pi} \frac{1}{e^{\hbar\omega/kT} - 1} = \frac{1}{2\pi} f(\omega, T), \quad (4)$$

where $f(\omega, T)$ is the Bose-Einstein distribution function at the reservoir temperature T . In order to evaluate (3), the eigensolutions $|v(\omega)\rangle$ of the open system have to be expressed in terms of a convenient basis made of a single phonon mode $|\psi_{i \in A}^{\text{in}}(\omega)\rangle$ coming from a reservoir A into the defect, and the set of phonon modes $\psi_j^{\text{out}}(\omega)$ coming out of the defect toward the reservoirs:

$$|v_i(\omega)\rangle = |\psi_i^{\text{in}}(\omega)\rangle + \sum_j S_{ji}(\omega) |\psi_j^{\text{out}}(\omega)\rangle + |v_i^{\text{def}}(\omega)\rangle, \quad (5)$$

where both defect displacements and reservoir surface states at the interfaces are included in $|v_i^{\text{def}}(\omega)\rangle$. The scattering tensor $\mathbf{S}(\omega)$ maps the incoming phonons $|\psi_i^{\text{in}}(\omega)\rangle$ onto the outgoing phonons $|\psi_j^{\text{out}}(\omega)\rangle$. As the energy carried by any incoming or outgoing phonon with frequency ω is quantized as $\hbar\omega$,

(3) provides the following normalization and orthogonality conditions:

$$\begin{aligned} \langle \psi_{i \in A}^{\text{in}}(\omega) | [\mathbf{P}_A, \mathbf{D}] | \psi_{j \in A}^{\text{in}}(\omega) \rangle &= -\frac{i\hbar}{2\pi} \cdot \delta_{ij}, \\ \langle \psi_{i \in A}^{\text{out}}(\omega) | [\mathbf{P}_A, \mathbf{D}] | \psi_{j \in A}^{\text{out}}(\omega) \rangle &= \frac{i\hbar}{2\pi} \cdot \delta_{ij}, \\ \langle \psi_{i \in A}^{\text{in}}(\omega) | [\mathbf{P}_A, \mathbf{D}] | \psi_{j \in A}^{\text{out}}(\omega) \rangle &= 0, \end{aligned} \quad (6)$$

where \mathbf{P}_A denotes the projector on reservoir A . Combining the stationary nonequilibrium weights of (4) with (3), and observing the conditions of (6), one obtains the stationary energy transfer between reservoirs A and B :

$$\Phi_{A \rightarrow B} = \int \frac{\hbar\omega}{2\pi} \sum_{i \in A} \sum_{j \in B} |S_{ij}(\omega)|^2 [f(\omega, T_A) - f(\omega, T_B)] d\omega. \quad (7)$$

Once $\mathbf{S}(\omega)$ is obtained by computing the eigenstates $|v(\omega)\rangle$, the energy flux between two reservoirs A, B is determined using the transmission coefficient $\mathcal{T}_{AB}(\omega) = \sum_{i \in A} \sum_{j \in B} |S_{ij}(\omega)|^2$. The corresponding thermal conductance is given by the Landauer formula as the limit of (7) when $T_A \rightarrow T_B$:

$$\sigma_{AB}(T) = \int \frac{\hbar\omega}{2\pi} \mathcal{T}_{AB}(\omega) \dot{f}(\omega, T) d\omega. \quad (8)$$

However, the derivation of these expressions is equivalent to that for the scattering boundary condition equation;³¹ it turns out useful to have a generalized expression of the energy transfer between arbitrary parts of the system for the implementation scheme outlined in the following section, and to treat systems with more than two semi-infinite reservoirs.

III. SCALABLE IMPLEMENTATION

The first step to obtain the eigenstates described in (5) consists of rewriting the open system eigenvalue equation as a null-space search problem:

$$\mathbf{D}v = \omega^2 v \quad \Leftrightarrow \quad v \in \ker\{\mathbf{D} - \omega^2\}. \quad (9)$$

One can consider a partition $\mathcal{P} = \{\mathbf{P}_i\}$ of the system, typically a set of projectors on each reservoir completed by a set of projectors on the defect, and solve the auxiliary equations:

$$v \in \ker\{\mathbf{P}_i(\mathbf{D} - \omega^2)\}. \quad (10)$$

Only the solutions defined within the interaction range of the current part need to be represented explicitly. A simple QR decomposition of the corresponding interaction matrix provides us with those solutions. The final eigenstates are then given by the intersection of the resulting invariant subspaces:

$$\mathbf{D}v = \omega^2 v \quad \Leftrightarrow \quad v \in \bigcap_P \ker\{\mathbf{P}_i(\mathbf{D} - \omega^2)\}. \quad (11)$$

As the intersection of two subspaces is defined by the degrees of freedom shared by their subsets, one can keep low memory usage and fast arithmetic by discarding the unnecessary coefficients.

Two different strategies are used during the reconstruction of the defect solutions: At first, a serial reconstruction takes place within each computer node. Starting from the solution set of a unique auxiliary equation, we repeatedly solve a

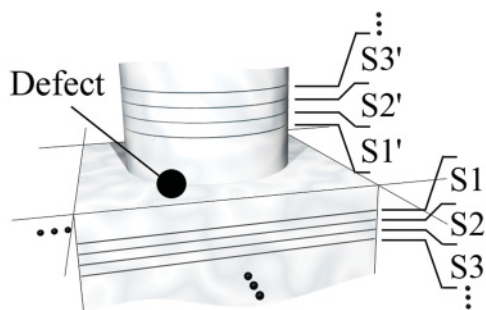


FIG. 1. Silicon nanowire and bulk interconnect partitioning. The central defect is generally further subdivided in order to speed up the computation. The bulk and wire reservoirs are organized as a pile of periodic slices (S and S' , respectively) indexed starting from the contact areas.

neighboring auxiliary equation and intersect the resulting subset with the current solution. This method allows low memory requirement within the node. Once all the auxiliary equations have been solved, the internodes reconstruction is achieved with two-by-two intersections of the neighboring subsets. This last strategy ensures a good scalability of the implementation: The reconstruction of the solutions in the unfavorable case of a spherical object of diameter R goes as $\mathcal{O}(R^6)$.

The reservoirs are treated in a separate way: As for the propagator method,³² every reservoir is partitioned in periodic slices S_i of dimension n such that only nearest neighbors interact (see Fig. 1). However, instead of formulating a spatial propagator, we first compute the $2n$ nontrivial solutions of Eq. (10) for the second slice $S2$ of the reservoir:

$$\mathbf{P}_{S2}(\mathbf{D} - \omega^2) \cdot \begin{pmatrix} v_{S1}^i \\ v_{S2}^i \\ v_{S3}^i \end{pmatrix} = 0. \quad (12)$$

Since any slice of the reservoir but $S1$ is equivalent to $S2$, the periodic solutions hold for the entire reservoir, except for $S1$ which is treated explicitly as part of the defect. The periodic solutions are then found through the $2n \times 2n$ generalized eigenproblem:

$$\alpha \begin{bmatrix} v_{S1}^1 \dots v_{S1}^{2n} \\ v_{S2}^1 \dots v_{S2}^{2n} \end{bmatrix} \cdot \begin{bmatrix} c_1 \\ \vdots \\ c_{2n} \end{bmatrix} = \beta \begin{bmatrix} v_{S2}^1 \dots v_{S2}^{2n} \\ v_{S3}^1 \dots v_{S3}^{2n} \end{bmatrix} \cdot \begin{bmatrix} c_1 \\ \vdots \\ c_{2n} \end{bmatrix}. \quad (13)$$

The intersection of the periodic solutions leads to the phonon modes $|\psi^{\text{in/out}}(\omega)\rangle$ ($|\alpha/\beta|=1$), and surfaces states ($|\alpha/\beta| \neq 1$). However, their reconstruction is straightforward and the intersection does not need to be performed explicitly, therefore one obtains

$$\mathbf{P}_{Sk} |\psi^{\text{in/out}}(\omega)\rangle = \left(\frac{\alpha}{\beta}\right)^{k-1} \sum_{i=1}^{2n} c_i |v_{S1}^i\rangle. \quad (14)$$

The intersection of the defect subset with the reservoir solutions leads to the decomposition of the open system eigenstates in terms of phonon modes. The eigenstates are

finally refined to extract the set $\{\tilde{v}_i\}$ spanning only surface states localized at the defect interface (i.e., with $|\alpha/\beta| < 1$):

$$\tilde{v}_i = \sum_j (\Lambda_{ji} |\psi_j^{\text{in}}(\omega)\rangle + \Gamma_{ji} |\psi_j^{\text{out}}(\omega)\rangle) + |\tilde{v}_i^{\text{def}}(\omega)\rangle. \quad (15)$$

The scattering tensor is easily obtained by applying the Λ^{-1} transform to $\{\tilde{v}_i\}$, providing the set of eigenstates $\{v_i\}$ defined in Eq. (5), so that $\mathbf{S}(\omega) = \Gamma \cdot \Lambda^{-1}$.

In the presence of short-range interatomic interactions, parts can be defined as small as the interaction range, so that only neighboring parts interact. Such implementation allows for efficient parallelization, in the same fashion as domain decomposition in molecular dynamics codes. Furthermore, a reciprocal space sampling technique allows for efficient treatment of the periodic reservoir solutions. Within this framework, the main limitation of the approach is the treatment of nonperiodic 1D reservoirs which requires the full diagonalization of a matrix growing as the surface of the contact.

IV. RESULTS AND DISCUSSION

a. Thermal conductance of bulk silicon and silicon nanowire contacts. We apply the scattering-matrix approach to compute the contact thermal resistance of a bulk-SiNW interface. Interface resistance plays an essential role in determining the thermal transport performance of nanostructured materials and nanoscale devices. In addition, evaluating the thermoelectric performances of nanostructures such as SiNWs, it is indispensable to be able to resolve the contact thermal resistance from the intrinsic resistance. A few special cases, such as grain boundaries in silicon, crystalline-amorphous interfaces, and silicon-germanium junctions, have previously been addressed using molecular dynamics and real-space Kubo-Greenwood formalism.^{35,36} An often overlooked yet omnipresent case where contact resistance is essential is the junction between nanostructures and reservoirs. A simplified model, based on lattice dynamics calculations of bulk silicon and of SiNWs with different diameters, predicts that the contact resistance is dominant over the intrinsic resistance of the ideal nanowire.^{37,38} Coherent contacts between crystals and nanowires with diameters as small as ~ 20 nm can be actually realized by etching nanowires directly out of the bulk precursor.^{39,40} We model the interatomic interactions between silicon atoms by means of the short-range empirical force field after Tersoff.⁴¹ Crystalline SiNWs with diameters between 2 and 14 nm are considered. The wires are grown in the (100) crystallographic direction, have a nearly circular cross section, and are coherently connected to the bulk reservoir. The surface is reconstructed in order to minimize the number of dangling bonds.⁴²

Transmission spectra are displayed in Fig. 2(a) along with the interface conductance σ [Fig. 2(b)] obtained by integrating the transmission coefficient over the whole frequency spectrum according to (8). The data sets are normalized according to the interface area, as one would reasonably expect the conductance of a junction to scale with its cross-section area. In fact such normalization makes curves comparable, but not overlapping. Normalized transmission spectra and $\sigma(T)$ curves overlap for wires of 7- and 10-nm diameter (red and pink curves in Fig. 2).

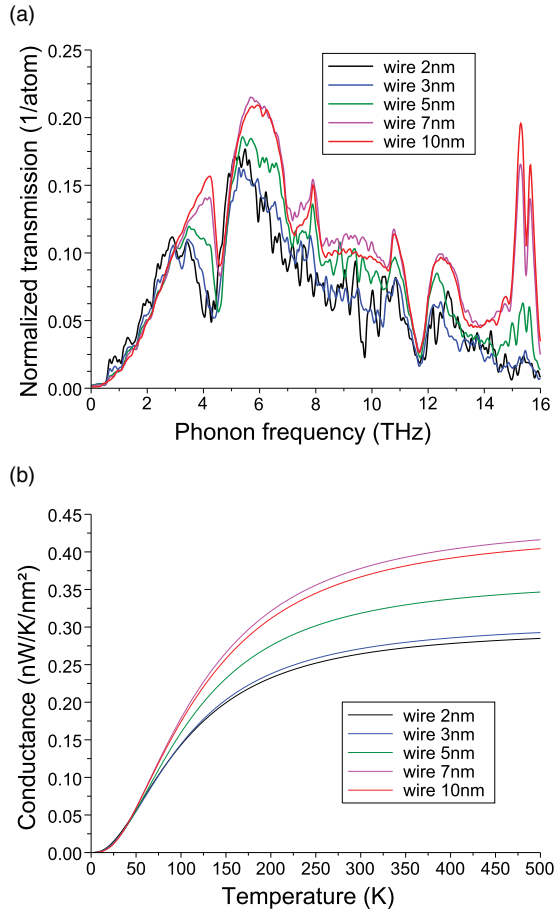


FIG. 2. (Color online) Transmission spectra (a) and thermal conductance as a function of the temperature (b) for a set of bulk-nanowire contacts. Both data sets are normalized with respect to the interface area expressed either in nm^2 (conductance) or in number of atoms at the contact interface (transmission).

This scaling laws are valid for frequencies larger than ~ 1 THz, when the number of channels on both sides of the junction becomes conspicuous. The transmission is roughly determined by the number of channels in the wire, scaled by a suitable average transmission coefficient which does not depend on the cross-section area of the wire. At frequencies lower than a certain threshold (0.56 THz for $d = 5$ nm, 0.4 THz for $d = 7$ nm, and 0.3 THz for $d = 10$ nm) one always finds four channels in the wire: namely, two flexure transverse acoustic (TA) modes with quadratic dispersion, one torsional and one longitudinal acoustic (LA) mode. Torsional modes are completely reflected by the interface. This shows that the availability of channels at a certain energy is not sufficient to guarantee transmission and that modes need to share the same character (i.e., similar polarization) to transfer energy across the interface. This determines the transmission spectra of the interfaces with thinner wires and, as will be discussed later, the scaling behavior of the reflection coefficients. Whereas heat transport in thicker wires can be treated within a mesoscopic approach,^{43,44} below the threshold diameter of 7 nm, one has to consider explicitly the atomistic details of the interface to obtain an accurate estimate of the contact conductance. As the construction of the bulk-wire interface is ideal at the atomic

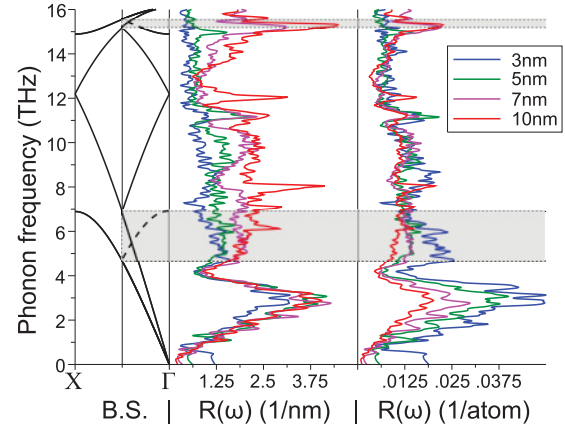


FIG. 3. (Color online) Band structure of the bulk contact (left panel) and reflection spectra of the nanowire modes normalized with respect to the diameter (center panel) and the surface area (right panel) of the SiNW.

scale, our calculations provide an upper limit to the contact conductance. In the low-temperature regime ($T < 50$ K) the interface area normalized contact conductances collapse to a single curve and display a temperature dependence of T^3 . This trend was formerly predicted analytically³⁸ and confirmed in experiments,³⁹ where it was shown that deviations from the T^3 behavior stem from specific features of the SiNW, such as surface roughness, the effects of which add up in series to the contact conductance.

On the other hand the reflection spectrum for modes coming from the wire displays more complex scaling, which provides useful insight in the physics of phonon scattering at the contact interface. The reflection spectra, normalized with respect to diameter and cross section of the SiNW, are shown in Fig. 3 (center and right panel). The reflection spectra scale with the diameter of the wires for low-frequency acoustic phonons, up to ~ 4.6 THz, which corresponds to the folding of the transverse acoustic (TA) band of bulk silicon. Since the number of channels is proportional to the interface area, this indicates a dependence of the average reflection coefficients on the size of the nanowire. The reflection coefficients are in turn an indicator of the mismatch of the phonons of the wire with those of the bulk. In fact, the average reflection coefficients decrease with the size of the wire, because the modes in the bulk and in the nanowire become more and more similar in larger wires, reducing the interfacial scattering. The linear dependence of the total reflection function on the diameter also reveals that these modes get scattered mainly at the perimeter of the contact interface. This is indeed confirmed by the real-space distribution of the energy flux discussed below. Between 4.6 and 7 THz we observe a transition between this scaling regime and the standard situation in which the reflection spectra scale with the interface area, which takes place above 7 THz. For frequencies larger than 7 THz the average reflection coefficients are relatively low, between 0.05 and 0.2, and do not depend on the diameter of the wires, so that the total reflection scales with the number of channels.

b. Representation of the heat flux. An advantage of the present implementation of the scattering-matrix method is that it provides a real-space representation of the energy

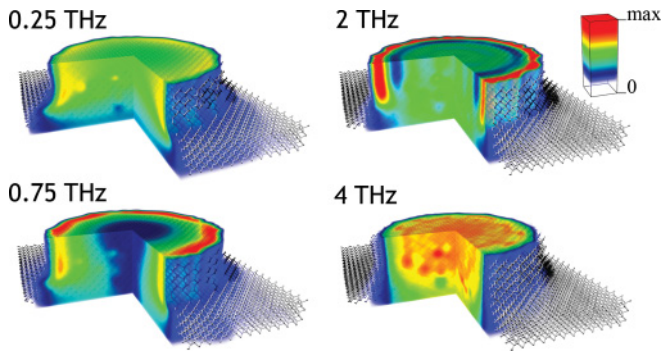


FIG. 4. (Color) Volumetric representation of the norm of the energy flux at the interface of a 10-nm-thick silicon nanowire, corresponding to channels with frequency of 0.25, 0.75, 2, and 4 THz. In the 0.75 and 2 THz case, thermal transport mainly occurs in a thin subsurface layer (red color area).

flux at any given frequency. This allows visualization of the parts of the system that primarily transmit or reflect thermal energy. An example is shown in Fig. 4, where the norm of the heat flux across a bulk 10-nm SiNW interface is represented. Phonon branches at 0.25, 0.75, 2, and 4 THz are considered. The spacial features of heat transport at different frequencies are clearly different: Whereas at the lowest frequency (0.25 THz) thermal energy is mainly transmitted through the central bulklike part of the wire, at higher frequencies (0.75 and 2 THz) thermal energy is transferred through a surface layer. Beyond 4 THz, heat is transferred through the center of the wire. We note that phonons with frequency between ~ 1 and ~ 4 THz, which are the majority heat carriers in crystalline Si at room temperature, transfer energy preferably through a subsurface layer. Therefore our results may hint at the reason why thermal conductivity of SiNW is very sensitive to surface modifications, such as disorder or presence of interfaces,^{8,45} however, this needs to be proved by calculations of rough wires.

c. Dimensionality and shape effects. In order to probe the effects of shape and dimensionality reduction on the contact conductance we compare the number of phonon channels (corresponding to the density of states) over the whole frequency spectrum, in contacts made of crystalline bulk silicon and either wires with a circular section or square rods. We only consider SiNW larger than the threshold size of 7 nm, identified as the onset for a mesoscopic theory of thermal transport. The calculations have been performed for SiNW with diameters up to 14 nm. The data are conveniently normalized with respect to the contact surface area and are compared to the number of channels in three-dimensional periodic bulk. To verify size convergence we consider two bulk samples with cubic supercell of 8.7 and 13 nm, respectively (Fig. 5). Our data show that for SiNWs larger than 7 nm, the number of channels per atom at a given frequency does not depend on the diameter. The number of channels at low frequency (< 3 THz) for the contacts is the same as in the crystalline bulk, but it deviates significantly from the bulk at larger frequencies. This means that even in contact interfaces with very large wires, one cannot expect to recover bulklike thermal conductance. It also indicates that dimensionality reduction has a profound effect on the limit density of states as

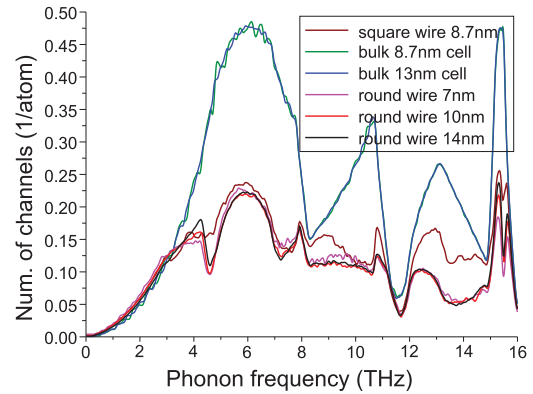


FIG. 5. (Color online) Number of transmission channels for a set of bulk-nanowire contacts of different diameter and shape. The data are normalized with respect to the interface area expressed in number of atoms. Data are compared to the number of channels in a three-dimensional periodic bulk to highlight the effect of dimensionality reduction. All the nanowires considered here are larger than the 7-nm diameter threshold.

well. Such a limit depends also on the shape of the SiNW, but to a minor extent. The spectrum of square-shaped nanorods differs from that of circular ones in the medium-to-high frequency range, but it retains similar features as cylindrical wires and does not seem to approach the three-dimensional (3D) bulk limit either.

V. CONCLUSIONS

We have developed an efficient method based on the scattering-matrix approach to compute the thermal conductance in an open system. Our derivation leads to an expression of the energy flux between semi-infinite reservoirs across a defect region, equivalent to the one derived in Refs. 18–20, and 31. We have implemented this expression with a stable partitioning and knitting algorithm that allows real-size devices to be simulated at the atomistic level. We have used this approach to compute the contact thermal conductance of ideal junctions between bulk silicon and silicon nanowires of different diameters. Our results show that in SiNW with circular cross section, with diameter of ~ 7 nm and larger, phonon transmission, reflection, and thermal conductance obey simple scaling laws, whereas deviations are observed for thinner wires. We have also investigated the effects of heat conduction on shape and dimensionality for wire diameters of 7 nm and beyond. Our approach also provides a direct space visualization of frequency-dependent heat flux, which yields valuable insight into the spatial features of heat conduction in nanoscale devices.

ACKNOWLEDGMENTS

Calculations were performed on the IBM Power6 system at the Rechenzentrum Garching. I.D. acknowledges support from the Multiscale Materials Modeling Initiative of the Max Planck Society. The authors thank K. Kremer, L. F. Pereira, and C. Joachim for useful suggestions, and L. Pavka for critical reading of the manuscript.

*duchemin@mpip-mainz.mpg.de

†donadio@mpip-mainz.mpg.de

- ¹C. Yu, L. Shi, Z. Yao, D. Li, and A. Majumdar, *Nano Lett.* **5**, 1842 (2005).
- ²S. Ghosh, W. Bao, D. L. Nika, S. Subrina, E. P. Pokatilov, C. N. Lau, and A. A. Balandin, *Nat. Mater.* **9**, 555 (2010).
- ³R. S. Prasher, X. J. Hu, Y. Chalopin, N. Mingo, K. Lofgreen, S. Volz, F. Cleri, and P. Koblinski, *Phys. Rev. Lett.* **102**, 105901 (2009).
- ⁴A. N. Volkov and L. V. Zhigilei, *Phys. Rev. Lett.* **104**, 215902 (2010).
- ⁵W. Li, H. Sevinçli, G. Cuniberti, and S. Roche, *Phys. Rev. B* **82**, 041410 (2010).
- ⁶R. Rurali, *Rev. Mod. Phys.* **82**, 427 (2010).
- ⁷A. I. Boukai, Y. Bunimovich, J. Tahir-Kheli, J.-K. Yu, W. A. Goddard, and J. R. Heath, *Nature (London)* **451**, 168 (2008).
- ⁸A. I. Hochbaum, R. Chen, R. D. Delgado, W. Liang, E. C. Garnett, M. Najarian, A. Majumdar, and P. Yang, *Nature (London)* **451**, 163 (2008).
- ⁹M. S. Dresselhaus, G. Chen, M. Y. Tang, R. Yang, H. Lee, D. Wang, Z. Ren, J.-P. Fleurial, and P. Gogna, *Adv. Mater.* **19**, 1043 (2007).
- ¹⁰G. Pernot, M. Stoffel, I. Savic, F. Pezzoli, P. Chen, G. Savelli, A. Jacquot, J. Schumann, U. Denker, I. Mönch, Ch. Deneke, O. G. Schmidt, J. M. Rampnoux, S. Wang, M. Plissonnier, A. Rastelli, S. Dilhaire, and N. Mingo, *Nat. Mater.* **9**, 491 (2010).
- ¹¹J.-K. Yu, S. Mitrovic, D. Tham, J. Varghese, and J. R. Heath, *Nature Nanotechnology* **5**, 718 (2010).
- ¹²J. Tang, H.-T. Wang, D. H. Lee, M. Fardy, Z. Huo, T. P. Russell, and P. Yang, *Nano Lett.* **10**, 4279 (2010).
- ¹³R. Landauer, *Phil. Mag.* **21**, 863 (1970).
- ¹⁴M. Buttiker, *Phys. Rev. B* **32**, 1846 (1985).
- ¹⁵N. S. Wingreen, A. P. Jauho, and Y. Meir, *Phys. Rev. B* **48**, 8487 (1993).
- ¹⁶T. N. Todorov, *Phys. Rev. B* **54**, 5801 (1996).
- ¹⁷M. Brandbyge, J. L. Mozos, P. Ordejon, J. Taylor, and K. Stokbro, *Phys. Rev. B* **65**, 165401 (2002).
- ¹⁸G. Fagas, A. G. Kozorezov, C. J. Lambert, J. K. Wigmore, A. Peacock, A. Poelaert, and R. den Hartog, *Phys. Rev. B* **60**, 6459 (1999).
- ¹⁹A. Ozpineci and S. Ciraci, *Phys. Rev. B* **63**, 125415 (2001).
- ²⁰D. Segal, A. Nitzan, and P. Hanggi, *J. Chem. Phys.* **119**, 6840 (2003).
- ²¹N. Mingo and L. Yang, *Phys. Rev. B* **68**, 245406 (2003).
- ²²I. Savic, N. Mingo, and D. A. Stewart, *Phys. Rev. Lett.* **101**, 165502 (2008).
- ²³T. Markussen, A.-P. Jauho, and M. Brandbyge, *Phys. Rev. B* **79**, 035415 (2009).
- ²⁴N. Mingo, *Phys. Rev. B* **74**, 125402 (2006).
- ²⁵K. Kazymyrenko and X. Waintal, *Phys. Rev. B* **77**, 115119 (2008).
- ²⁶D. A. Areshkin and B. K. Nikolic, *Phys. Rev. B* **81**, 155450 (2010).
- ²⁷D. Donadio and G. Galli, *Phys. Rev. Lett.* **102**, 195901 (2009).
- ²⁸D. Donadio and G. Galli, *Nano Lett.* **10**, 847 (2010).
- ²⁹D. A. Young and H. J. Maris, *Phys. Rev. B* **40**, 3685 (1989).
- ³⁰H. Zhao and J. B. Freund, *J. Appl. Phys.* **97**, 024903 (2005).
- ³¹J. Wang and J.-S. Wang, *Phys. Rev. B* **74**, 054303 (2006).
- ³²P. Sautet and C. Joachim, *Phys. Rev. B* **38**, 12238 (1988).
- ³³S. Ami and C. Joachim, *Phys. Rev. B* **65**, 155419 (2002).
- ³⁴P. Sautet and C. Joachim, *Chem. Phys. Lett.* **185**, 23 (1991).
- ³⁵A. Bodapati, P. K. Schelling, S. R. Phillpot, and P. Koblinski, *Phys. Rev. B* **74**, 245207 (2006).
- ³⁶E. S. Landry and A. J. H. McGaughey, *Phys. Rev. B* **80**, 165304 (2009).
- ³⁷Y. Chalopin, J. N. Gillet, and S. Volz, *Phys. Rev. B* **77**, 233309 (2008).
- ³⁸C. M. Chang and M. R. Geller, *Phys. Rev. B* **71**, 125304 (2005).
- ³⁹J. S. Heron, T. Fournier, N. Mingo, and O. Bourgeois, *Nano Lett.* **9**, 1861 (2009).
- ⁴⁰K. Hippalgaonkar, B. Huang, R. Chen, K. Sawyer, P. Ercius, and A. Majumdar, *Nano Lett.* **10**, 4341 (2010).
- ⁴¹J. Tersoff, *Phys. Rev. B* **39**, 5566 (1989).
- ⁴²T. Vo, A. J. Williamson, and G. Galli, *Phys. Rev. B* **74**, 045116 (2006).
- ⁴³D. E. Angelescu, M. C. Cross, and M. L. Roukes, *Superlattices Microstruct.* **23**, 673 (1998).
- ⁴⁴R. S. Prasher and P. E. Phelan, *J. Appl. Phys.* **100**, 063538 (2006).
- ⁴⁵M. Hu, K. P. Giapis, J. V. Goicochea, X. Zhang, and D. Poulidakos, *Nano Lett.* **11**, 618 (2011).